

Topology optimization of lightweight periodic lattices under simultaneous compressive and shear stiffness constraints



Alireza Asadpoure, Lorenzo Valdevit*

Mechanical and Aerospace Engineering, University of California Irvine, Irvine, CA 92697, USA

ARTICLE INFO

Article history:

Received 5 February 2014

Received in revised form 2 October 2014

Available online 4 February 2015

Keywords:

Elastic properties

Topology optimization

Periodic lattices

Micro-architected materials

Lightweight materials

ABSTRACT

This paper investigates the optimal architecture of planar micro lattice materials for minimum weight under simultaneous axial and shear stiffness constraints. A well-established structural topology optimization approach is used, where the unit cell is composed of a network of beam elements (Timoshenko beams are used instead of truss elements to allow modeling of bending-dominated architectures); starting from a dense unit cell initial mesh, the algorithm progressively eliminates inefficient elements and resizes the essential load-bearing elements, finally converging to an optimal unit cell architecture. This architecture is repeated in both directions to generate the infinite lattice. Hollow circular cross-sections are assumed for all elements, although the shape of the cross-section has minimal effect on most optimal topologies under the linear elasticity assumption made throughout this work. As optimal designs identified by structural topology optimization algorithms are strongly dependent on initial conditions, a careful analysis of the effect of mesh connectivity, unit cell aspect ratio and mesh density is conducted. This study identifies hierarchical lattices that are significantly more efficient than any isotropic lattice (including the widely studied triangular, hexagonal and Kagomé lattices) for a wide range of axial and shear stiffness combinations. As isotropy is not always a design requirement (particularly in the context of sandwich core design, where shear stiffness is generally more important than compressive stiffness), these optimal architectures can outperform any established topology. Extension to 3D lattices is straightforward.

© 2015 Elsevier Ltd. All rights reserved.

1. Introduction

Metallic cellular materials possess unique combinations of low weight, high stiffness and strength, and enable substantial energy absorption at relatively low crushing stress (Evans et al., 2001, 2010). Additionally, when designed with interconnected porosity, the open volume in the architecture can be exploited for active cooling or energy storage, providing unique opportunities for multifunctionality (Valdevit et al., 2006a; Bell et al., 2005). These attributes make metallic cellular solids uniquely suited as cores of sandwich structures for applications ranging from lightweight aerospace structures to blast-resistant armors (for both land and sea vehicles) (Evans et al., 2010; Wadley et al., 2010), and actively cooled panels for combustor walls of next-generation hypersonic vehicles (Valdevit et al., 2011, 2008). From a mechanical standpoint, the core of a well-designed sandwich panel needs to possess excellent shear stiffness and strength (to support the internal shear

force that develops under transverse loads on the panel) as well as compressive stiffness and strength along the through-thickness direction of the panel (to resist indentation under concentrated transverse loads) (Allen, 1969).

At a given relative density (defined as the mass density of the cellular medium divided by the mass density of the solid constituent), topologically architected cellular structures (e.g., periodic architectures) are vastly superior to stochastic foams, by virtue of a more efficient stress transfer mechanism between the macroscale and the unit-cell level: when appropriately designed, each unit-cell element (whether a truss or a shell feature) will largely experience tension or compression under the applied external loads, with minimal bending (Evans et al., 2001; Deshpande et al., 2001). This guarantees full exploitation of the mechanical properties of the base material, providing the cellular material exceptional mechanical efficiency (in terms of specific stiffness and strength). Over the past decade, a number of cellular topologies were investigated and characterized, ranging from truss-like concepts (Deshpande et al., 2001; Zok et al., 2003, 2004) to prismatic (honeycomb-type) designs (Valdevit et al., 2004; Zok et al., 2005). Prismatic designs with the channels in the plane of the sandwich panel (hence

* Corresponding author. Tel.: +1 949 824 4173; fax: +1 949 824 8585.

E-mail address: valdevit@uci.edu (L. Valdevit).

offering open porosity) can be thought of as two-dimensional topologies, extruded in the third direction. The most common 2D topologies are hexagonal, triangular, and Kagomé designs, regular lattices in which all elements have the same length (Gibson and Ashby, 1999; Christensen, 1995). The effective mechanical properties of these simple lattices are readily extracted in analytical form. Importantly, because of the threefold symmetry, all three designs are in-plane isotropic.

Although isotropy is a desirable property in a number of applications, it is not essential (or even advantageous) for the core of a sandwich panel: appropriately tailoring the anisotropy (e.g., independently choosing compressive and shear stiffness and strength) may in principle result in much more weight efficient designs. Besides isotropy, the choice of periodic architectures with simple unit cells and very few length scales was traditionally justified by manufacturability requirements. Recently, with the development and advancement of a plethora of additive manufacturing techniques (e.g., stereolithography, select laser sintering, direct metal manufacturing (Gibson et al., 2010), SPPW-based manufacturing (Schaedler et al., 2011; Jacobsen et al., 2007)), the ability to fabricate extremely complex and hierarchical architectures has been rapidly growing.

In most studies, optimal designs of lightweight cellular materials have been identified by optimizing the geometric parameters of a predefined lattice-type architecture (Valdevit et al., 2004, 2006b). Although this technique allows analytical description for appropriately chosen topologies, it relies on the intuition of the designer in the selection of the lattice topology. Topology optimization presents a more elegant approach (Caldman et al., 2013). In its classic continuum form, a unit cell is meshed with finite elements, each of which can be assigned either of two phases (e.g., solid and void). The optimizer progressively reassigns elements until an optimal phase distribution is achieved. Design of cellular materials has been greatly investigated using topology optimization method, for example, by Sigmund (1995) in design of materials with prescribed mechanical properties, Sigmund and Torquato (1997) in design of multiphase materials for extreme thermal expansion, Silva et al. (1997) in design of piezoelectric microstructures, Dobson and Cox (1999) for design of photonic crystals for band-gaps, and Sigmund and Jensen (2003) for design of materials and structures for phononic band-gaps. Further elaborations of this technique, such as multi-scale optimal design (Liu et al., 2008), analysis of the effects of boundaries (Yan et al., 2006), and optimal design of isotropic cellular solids with prescribed effective moduli and conductivity (Hyun and Torquato, 2002) have been presented. Recently, more complicated materials systems have been analyzed, for example functionally graded materials with desired effective properties (Paulino et al., 2009), and materials with prescribed nonlinear properties (Wang et al., 2014).

Although extremely powerful, continuum topology optimization does not guarantee that the optimal topology be a lattice design. If this is desired, truss-like (or discrete as opposed to continuum) topology optimization is the ideal approach. Starting from a dense mesh of lattice members (Dorn et al., 1964) for a unit cell, truss (or beam)-based topology optimization seeks the best connectivity by removing inefficient elements and resizing the cross-section of the most efficient ones. See Bendsøe and Sigmund (2003) and Rozvany (1996) for more details on topology optimization of truss-like structures. This technique was first applied to the optimization of effective properties of a cellular medium (inverse homogenization) in Sigmund (1994); recently, Asadpoure et al. (2014) extended this approach to integrate the fabrication cost of lattices in the objective function.

In this context, this article numerically investigates the minimum-density designs of periodic 2D lattices under arbitrary combinations of prescribed axial (e.g., compressive) and shear moduli.

Optimal lattice architectures are extracted using a formal structural topology optimization algorithm, and the stiffnesses of each design are calculated via the finite element method, utilizing beam elements to model all lattice members. Given the intense recent interest in hollow micro-lattices as an architecture that could provide exceptionally low density and a wide length scale hierarchy (Schaedler et al., 2011; Valdevit et al., 2013; Maloney et al., 2013), in all the calculations the cross-section of each lattice member is assumed to be circular and hollow. However, because most optimal designs support loads primarily by axial deformation (as opposed to bending) of the members, the actual shape of the cross-section has minimal effect on the results (see Section 3.2).

The article is presented as follows. Section 2 defines the minimum relative density problem with axial and shear elastic constraints on a unit cell of the lattice. The unit cell consists of Timoshenko beam elements with hollow circular cross-section, whose existence, thickness, and radius are modeled as continuous design variables, in order to take advantage of gradient-based optimizers. The finite element analysis, including the required boundary conditions for obtaining axial and shear moduli, are presented in Section 2.2. The sensitivity analysis required for the gradient-based optimizer is derived in Section 2.3, followed by the details of the algorithm used for the topology optimization in Section 2.4. Optimized solutions, compared to the well-known bounds on isotropic cellular materials and with the most commonly available 2D lattices (triangular, hexagonal and Kagomé designs), are presented in Section 3. In the same section, the effects of lattice hierarchy is discussed. Conclusions follow. The appendices include a mesh sensitivity analysis, discussing the effect of initial mesh density, domain shape and upper bound on the lattice member radius.

2. The topology optimization problem

2.1. Problem statement

The objective of the optimization is to find the minimum weight of a two-dimensional periodic lattice material under simultaneous axial and shear stiffness constraints, i.e. the optimized lattice maintains a minimum axial stiffness as well as a minimum shear stiffness. A structural topology optimization algorithm is used. The unit cell of the lattice is initially seeded with a dense mesh of structural finite elements; beam elements are used as opposed to truss elements, in order to allow load carrying by bending rather than solely by axial deformation. Although optimally designed lattices are almost always statically determinate (and hence carry load by axial deformation of each member), allowing for bending deformation might be important for extremely anisotropic designs where the required axial and shear stiffness are vastly different. As the optimization procedure progresses, inefficient elements are eliminated and the cross-sections of the remaining elements are resized, ultimately converging to the optimal minimum-density lattice architecture. A binary design variable, x_x^e , is assigned to each lattice element to represent its existence (i.e., $x_x^e = 1$ if the element e exists, otherwise $x_x^e = 0$). The need for the introduction of this additional variable is explained later in this section. The formal optimization problem on a discretized domain Ω (representing a unit cell or fraction thereof) can be expressed as follows:

$$\min_{\mathbf{x}} \bar{\rho}(\mathbf{x}) = \sum_{v \in \Omega} \frac{x_x^e v^e(\mathbf{x}_c)}{V^\Omega} \quad (1)$$

$$s.t. \quad C_E^\Omega(\mathbf{x}) \leq C_E^* \quad (2)$$

$$C_G^\Omega(\mathbf{x}) \leq C_G^* \quad (3)$$

$$x_x^e = \begin{cases} 1 & \text{if solid} \\ 0 & \text{if void} \end{cases}, \quad \forall e \in \Omega \quad (4)$$

where \mathbf{x} is the vector of design variables, consisting of the binary variables for existence of elements (\mathbf{x}_x) and the real design variables defining the cross-section (\mathbf{x}_c); $\bar{\rho}(\mathbf{x})$ is the relative density of the lattice, V^Ω is the volume of the design domain Ω ; v^e is the volume of the element e ; C_E^Ω and C_G^Ω are the compliances of the design domain under uniaxial compressive and shear states of stress, respectively; and C_E^* and C_G^* are upper bounds on the compliances, consistent with the prescribed axial and shear stiffness requirements (see Section 2.2.2 for details). The notations $v^e(\mathbf{x}_c^e)$, $C_E^\Omega(\mathbf{x})$, and $C_G^\Omega(\mathbf{x})$ are used to emphasize dependence on the design variables in Eqs. (1)–(4). Geometric constraints must be applied to fully complete the formulation. Although the method for this investigation can be applied to any cross sectional shapes, we restrict the problem to designing periodic micro-structures consisting of circular hollow tube elements. The cross-section of each element can thus be represented by two design variables, radius and thickness. For this section, one obvious design constraint is that the thickness of an element e (t^e) must be less than or equal to its radius (r^e). To avoid imposing varying bounds on one of the design variables for every element (which would require additional constraints with the chosen optimizer – see Section 2.4), the thickness of each element is defined as a fraction of its radius, i.e.

$$t^e(x_t^e, r^e) = x_t^e r^e \quad (5)$$

where x_t^e is the design variable for thickness of element e , and is defined between 0 and 1. In order to keep all the design variables between 0 and 1, the radius of element e can be represented by

$$r^e(x_r^e) = r_{max} x_r^e \quad (6)$$

where r_{max} is the maximum radius and $x_r^e \in [0, 1]$ is the design variable for the radius of element e . In summary, the entire design variable for element e can be expressed in vector form as:

$$\mathbf{x}^T = \{\mathbf{x}_x^T \mathbf{x}_c^T\} \quad (7)$$

$$= \{\mathbf{x}_x^T \mathbf{x}_t^T \mathbf{x}_r^T\} \quad (8)$$

where $\mathbf{x}_c^T = \{\mathbf{x}_t^T \mathbf{x}_r^T\}$ are design variables associated with the geometric parameters of cross-sections (thickness and radius).

The optimization problem stated by Eqs. (1)–(4) is dependent on the constituent material. This dependence can be eliminated by scaling $W^\Omega(\mathbf{x})$, $C_E^\Omega(\mathbf{x})$, C_E^* , $C_G^\Omega(\mathbf{x})$, and C_G^* with the corresponding values for the solid design domain filled with the constituent material.

Solving the optimization problem described above for a combination of discrete variables (\mathbf{x}_x) and continuous variables (\mathbf{x}_c and \mathbf{x}_r) for a large-scale problem is cumbersome. To enable the use of gradient-based (GB) optimizers and thus dramatically reduce the numerical complexity, the binary constraint in Eq. (4) is relaxed, i.e., x_x^e is allowed to take any values in the $[0, 1]$ interval. The convergence to intermediate values between 0 and 1 is then penalized using the Solid Isotropic Material with Penalization (SIMP) method (Bendsøe, 1989; Rozvany et al., 1992). The following SIMP method is utilized:

$$E^e(x_x^e) = E_{min} + (x_x^e)^\eta (E - E_{min}) \quad (9)$$

where E is the Young's modulus of the constituent material (assumed to be the same for all elements), E^e is the Young's modulus of element e , E_{min} is a small number to keep the stiffness matrix positive definite when $x_x^e = 0$, and η is the penalizing exponent. As η approaches a large number, e.g. 5, the intermediate densities become inefficient. For example, suppose $\eta = 3$ and $x_x^e = 0.5$. This penalizing model reduces the stiffness to about one fourth of the original stiffness; but it does not have any effects on the volume fractions in Eq. (1). Therefore, retaining elements with intermediate volume fractions becomes inefficient. This model thus helps opti-

mizers approach a 0/1 solution. It is worth mentioning that this penalization strategy is only appropriate for binary variables, or generally variables that should take one of only two possible values in the final solution. The variables \mathbf{x}_t and \mathbf{x}_r are not necessarily at their bounds in the optimal solution (a wide range of element areas should be allowed); thus, penalizing these variables with this approach would unreasonably bias the optimal design toward solutions with only extremely small or extremely large elements. This justifies the introduction of \mathbf{x}_x as the penalization variable. One should nevertheless note that there is no guarantee that existing GB methods converge to global minima; rather, they may capture local minima. Among these local minima, some of them may be more desirable. For example, solutions with fewer elements may be of interest for ease of fabrication. To bias the optimizer towards solutions with relatively few elements, a penalty function can be added to the objective function in Eq. (1) as follows:

$$\min_{\mathbf{x}} (1 + \omega_p n_{el}(\mathbf{x}_x)) \bar{\rho}(\mathbf{x}) = (1 + \omega_p n_{el}(\mathbf{x}_x)) \sum_{\forall e \in \Omega} \frac{x_x^e v^e(\mathbf{x}_c)}{V^\Omega} \quad (10)$$

$$s.t. C_E^\Omega(\mathbf{x}) \leq \alpha_E \bar{C}_E \quad (11)$$

$$C_G^\Omega(\mathbf{x}) \leq \alpha_G \bar{C}_G \quad (12)$$

$$0 \leq x_x^e \leq 1 \quad \forall e \in \Omega \quad (13)$$

$$0 < x_{min} \leq x_t^e \leq 1 \quad \forall e \in \Omega \quad (14)$$

$$0 < x_{min} \leq x_r^e \leq 1 \quad \forall e \in \Omega \quad (15)$$

where \bar{C}_E and \bar{C}_G are the compliances of the design domain entirely filled with the constituent material and subjected to uniaxial compressive and shear states of stress, respectively (see Section 2.2.2 for details), α_E and α_G express the prescribed minimum relative axial and shear stiffness in non-dimensional form, respectively, ω_p is a penalizing weight for existence of each element, $n_{el}(\mathbf{x}_x)$ is the number of existing elements (i.e., elements for which $x_x^e > 0$), and x_{min} is a small number to keep the stiffness matrix positive definite. In these equations, $n_{el}(\mathbf{x}_x)$ should be differentiable, since we aim to use a GB optimizer. Therefore, a regularized Heaviside step function can be used to make $n_{el}(\mathbf{x}_x)$ a smooth function, defined as follows:

$$n_{el}(\mathbf{x}_x) = \sum_{\forall e \in \Omega} H(x_x^e) \quad (16)$$

where H is the regularized Heaviside step function (Guest et al., 2004) as

$$H(x_x^e) = 1 - \exp(-\beta x_x^e) + x_x^e \exp(-\beta) \quad (17)$$

When β approaches infinity, the above function approximates the Heaviside function more and more accurately. One may thus start with a small value of β , for example 1, and gradually increase this parameter to a large value, for example 100, to gradually penalize smaller values of x_x^e .

2.2. Finite element formulation

2.2.1. Theory

The elastic stiffness (axial and shear) of the periodic lattice is calculated with the finite elements method. The procedure is fully general and is applicable to both two-dimensional and three-dimensional lattices, with appropriate choices of boundary conditions. As mentioned before, beam elements are used throughout to model axial and flexural deformation of each lattice member. Once the global stiffness matrix \mathbf{K} is assembled, the unknown nodal displacements and reaction forces can be obtained solving the following linear problem:

$$\begin{bmatrix} \mathbf{K}_{ff}(\mathbf{x}) & \mathbf{K}_{fg}(\mathbf{x}) \\ \mathbf{K}_{gf}(\mathbf{x}) & \mathbf{K}_{gg}(\mathbf{x}) \end{bmatrix} \begin{bmatrix} \mathbf{d}_f(\mathbf{x}) \\ \mathbf{d}_g(\mathbf{x}) \end{bmatrix} = \begin{bmatrix} \mathbf{f}_f(\mathbf{x}) \\ \mathbf{f}_g(\mathbf{x}) \end{bmatrix} \quad (18)$$

where \mathbf{K} is the stiffness matrix, \mathbf{d} is the displacement vector, \mathbf{f} is the force vector, and subscripts f and g correspond to degrees of freedom that are free and prescribed, respectively. In Eq. (18), \mathbf{d}_f and \mathbf{f}_g (reactions) are unknown. We first solve the equation for \mathbf{d}_f , i.e. $\mathbf{K}_{ff}\mathbf{d}_f = \mathbf{f}_f - \mathbf{K}_{fg}\mathbf{d}_g$; subsequently, \mathbf{f}_g can be easily obtained by the second equation, i.e. $\mathbf{f}_g = \mathbf{K}_{gf}\mathbf{d}_f + \mathbf{K}_{gg}\mathbf{d}_g$.

Although the algorithm generally converges to a unit cell architecture comprising very slender members, the initial dense mesh can incorporate stocky elements (i.e., elements with a slenderness ratio < 5). As shear deformation can be significant for these (thick) elements, Timoshenko beam theory is used to obtain bending stiffness. The following shear coefficient is recommended for hollow tubes to accurately model shear deformation (Cowper, 1966):

$$\kappa_G^e = \frac{6(1+\nu)(1+\alpha_r^e)^2}{(7+6\nu)(1+\alpha_r^e)^2 + (20+12\nu)\alpha_r^e} \quad (19)$$

where κ_G^e is the shear coefficient for element e , ν is the Poisson's ratio of the constituent material, and $\alpha_r^e = 1 - t^e/r^e$.

2.2.2. Compliance calculations

Once the nodal displacements and the reaction forces are obtained from Eq. (18), the compliance of a design within design domain Ω can be calculated with the following generalized formulation (Niu et al., 2011)

$$C^\Omega(\mathbf{x}) = \mathbf{f}_f^T(\mathbf{x})\mathbf{d}_f(\mathbf{x}) - \mathbf{f}_g^T(\mathbf{x})\mathbf{d}_g \quad (20)$$

This formulation can be used for both axial and shear stiffness, with the appropriate choice of applied displacements and boundary conditions. For generality, the boundary conditions are presented in three dimensions, rendering the algorithm presented herein capable of optimizing 3D lattices. Reduction to the 2D case is trivial and is represented in Fig. 1. A prismatic unit cell is assumed, with dimensions L_x , L_y , and L_z along the X , Y , and Z directions, respectively. As the desired unit cell architecture is required to have reflection symmetry about the X , Y , and Z axes, the design domain Ω is chosen as one eighth (one quarter for 2D case) of the lattice unit cell. The compliance of the design domain under uniaxial loading along the Y direction can be calculated with the following prescribed displacements and boundary conditions (Li, 2008):

$$\begin{aligned} u_x|_{x=0} &= 0, & u_x|_{x=L_x^\Omega} &= \epsilon_{xx}L_x^\Omega \\ u_y|_{y=0} &= 0, & u_y|_{y=L_y^\Omega} &= \epsilon_{yy}L_y^\Omega \\ u_z|_{z=0} &= 0, & u_z|_{z=L_z^\Omega} &= \epsilon_{zz}L_z^\Omega \end{aligned} \quad (21)$$

where u_x , u_y , and u_z are translational degrees of freedom along X , Y , and Z , respectively, L_x^Ω , L_y^Ω , and L_z^Ω are the dimensions of the design domain Ω and ϵ_{xx} , ϵ_{yy} and ϵ_{zz} are the normal strains along X , Y , and Z , respectively. It should be noted that ϵ_{yy} is the prescribed (applied) uniform strain along the Y axis, whereas ϵ_{xx} and ϵ_{zz} are the resulting uniform strains along the X and Z axes required to ensure a one-dimensional state of stress along the Y direction. In FEM modeling, only one equation number (degree of freedom number) is used for all translational degrees of freedom along these directions at $X = L_x^\Omega$ and $Z = L_z^\Omega$ in order to ensure a uniform strain distribution at these boundaries. The rotational degrees of freedom are chosen to be compatible with the translational degrees of freedom for axial stiffness at these boundaries and are as follows:

$$\begin{aligned} \theta_{y,z}|_{x=0} &= 0, & \theta_{y,z}|_{x=L_x^\Omega} &= 0 \\ \theta_{x,z}|_{y=0} &= 0, & \theta_{x,z}|_{y=L_y^\Omega} &= 0 \\ \theta_{x,y}|_{z=0} &= 0, & \theta_{x,y}|_{z=L_z^\Omega} &= 0 \end{aligned} \quad (22)$$

where θ_x , θ_y , and θ_z are rotational degrees of freedom about the X , Y , and Z axes, respectively. With this choice of boundary conditions, satisfying the constraint in Eq. (11) is exactly equivalent to prescribing a minimum for the Young's modulus of the lattice (E_{lattice}), i.e. $\alpha_E \leq E_{\text{lattice}}/E$, with E the Young's modulus of the constituent material.

The compliance of the design domain under uniaxial shear in the XY plane (i.e., lateral translation in the X direction of the plane $Y = L_y^\Omega$) can be calculated with the following prescribed displacements and boundary conditions (Li, 2008):

$$\begin{aligned} u_{y,z}|_{x=0} &= 0, & u_{y,z}|_{x=L_x^\Omega} &= 0 \\ u_{x,z}|_{y=0} &= 0, & u_x|_{y=L_y^\Omega} &= \gamma_{yx}L_y^\Omega, & u_z|_{y=L_y^\Omega} &= 0 \\ u_z|_{z=0} &= 0, & u_z|_{z=L_z^\Omega} &= 0 \end{aligned} \quad (23)$$

and their corresponding compatible rotational degrees of freedom are

$$\begin{aligned} \theta_x|_{x=0} &= 0, & \theta_x|_{x=L_x^\Omega} &= 0 \\ \theta_y|_{y=0} &= 0, & \theta_y|_{y=L_y^\Omega} &= 0 \\ \theta_{x,y}|_{z=0} &= 0, & \theta_{x,y}|_{z=L_z^\Omega} &= 0 \end{aligned} \quad (24)$$

With this choice of boundary conditions, satisfying the inequality in Eq. (12) is exactly equivalent to imposing a minimum for the shear modulus of the lattice (G_{lattice}), i.e., $\alpha_G \leq G_{\text{lattice}}/G$, with G the shear modulus of the constituent material.

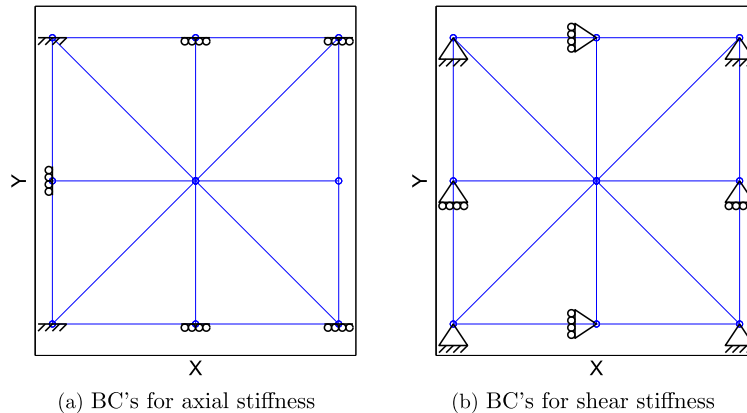


Fig. 1. Boundary Conditions (BC) for a 2D lattice used to evaluate (a) Compliance corresponding to the axial stiffness constraint, using uniform prescribed translation along Y direction at $Y = L_y^\Omega$; (b) Compliance corresponding to the shear stiffness constraint, using uniform prescribed translation along the X direction at $Y = L_y^\Omega$.

While the boundary conditions presented in Eqs. (21)–(22) and Eqs. (23)–(24) allow enforcement of axial and shear stiffness constraints along specific directions, one can easily retrieve boundary conditions for all other stiffness components.

It is however worth noting that only half of the weight and stiffness of elements whose both ends lie at the same boundary should be considered in Eqs. (10)–(12), as these elements are shared with other unit cells within a periodic lattice. Boundary conditions presented in Eqs. (21)–(22) and Eqs. (23)–(24) are individually applied to the lattice to evaluate Eqs. (11) and (12), respectively.

Fig. 1 illustrates the boundary conditions required to model 1/4 of a 2D design domain for evaluating the axial compliance along Y axis and shear compliance in the plane XY . Therefore, u_z and $\theta_{x,y}$ are inactive for these boundary conditions. Again, notice that although the translational degrees of freedom at $X = L_x^\Omega$ in Fig. 1(a) are free, a single equation number should be used for these degrees of freedom to ensure uniform strain along the X direction.

It is worth mentioning that the proposed approach for the extraction of axial and shear moduli only requires two analyses, while the conventional homogenization approach (Bourgat, 1979; Guedes and Kikuchi, 1990; Sigmund, 1994) requires 3 and 6 distinct analyses in 2D and 3D respectively, to fully characterize the unit cell elastic properties. Furthermore, the proposed approach allows modeling one quarter of unit cell; given that the cost of inverting the stiffness matrix is cubic in the number of degrees of freedom, this reduces the computational cost 64-fold ($1/4^3$). Therefore, compared to the classic homogenization algorithm, the proposed approach decreases the computational cost by roughly two orders of magnitudes, i.e. $2/3 \times 1/4^3$; the advantage would be even larger in 3D.

2.3. Sensitivities with respect to design variables

The Method of Moving Asymptotes (MMA) (Svanberg, 1987, 1995) is used to solve the structural topology optimization problem. As in any gradient-based (GB) approach, the key step in the optimization process is efficiently computing derivatives of the objective functions and constraints. Since topology optimization problems are commonly large-scale, using traditional numerical methods such as the finite difference method is not numerically efficient. We thus use an analytical method to compute derivatives efficiently.

In deriving the derivatives of functions in Eqs. (10)–(12) with respect to design variables, two groups of functions can be recognized. One group is explicitly a function of design variables, for which derivatives are straightforward to compute. In Eq. (10), n_{el} and \bar{p} are explicitly functions of design variables, i.e. \mathbf{x} , and their derivatives with respect to x^e are:

$$\frac{dn_{el}}{dx_x^e} = \beta \exp(-\beta x_x^e) + \exp(-\beta) \quad (25)$$

$$\frac{dn_{el}}{dx_i^e} = 0, \quad i = r, t \quad (26)$$

$$\frac{d\bar{p}}{dx_x^e} = \frac{v^e}{V^\Omega} \quad (27)$$

$$\frac{d\bar{p}}{dx_i^e} = \frac{x_x^e}{V^\Omega} \frac{dv^e}{dx_i^e}, \quad i = r, t \quad (28)$$

where d/dx_i^e denotes the (full) derivative with respect to x_i^e . The dependence on design variables (\mathbf{x}) in these equations is dropped for simplicity. The second group contains functions that are not explicitly dependent on the design variables. For example, C^Ω in Eq. (20) is a function of \mathbf{d}_f that is a function of inverse of \mathbf{K}_{ff} . This

implicit dependence makes computation of the derivatives cumbersome. For such a function, we use the adjoint method and consequently take the derivative of the function with addition of the equilibrium equation with an arbitrary constant vector λ , i.e.

$$\frac{dC^\Omega}{dx_i^e} = \frac{d}{dx_i^e} \left(C^\Omega + \lambda^T (\mathbf{K}_{ff} \mathbf{d}_f + \mathbf{K}_{fg} \mathbf{d}_g - \mathbf{f}_f) \right), \quad i = x, r, t \quad (29)$$

By substituting Eq. (20) and Eq. (18) for \mathbf{f}_g into Eq. (29), and after some manipulations, this equation can be rewritten as:

$$\begin{aligned} \frac{dC^\Omega}{dx_i^e} = & \left(\frac{d\mathbf{f}_f^T}{dx_i^e} - \mathbf{d}_g^T \frac{d\mathbf{K}_{fg}}{dx_i^e} \right) (\mathbf{d}_f - \lambda) + \lambda^T \frac{d\mathbf{K}_{ff}}{dx_i^e} \mathbf{d}_f - \mathbf{d}_g^T \frac{d\mathbf{K}_{gg}}{dx_i^e} \mathbf{d}_g \\ & + \frac{d\mathbf{d}_f^T}{dx_i^e} (\mathbf{K}_{ff} \lambda - (\mathbf{f}_f - \mathbf{K}_{fg} \mathbf{d}_g)), \quad i = x, r, t \end{aligned} \quad (30)$$

To avoid computation of $d\mathbf{d}_f/dx_i^e$, the last term on the right hand side of Eq. (30) can be eliminated by choosing λ as:

$$\lambda = -\mathbf{K}_{ff}^{-1} (\mathbf{f}_f - \mathbf{K}_{fg} \mathbf{d}_g) = -\mathbf{d}_f \quad (31)$$

Eq. (29) can then be rewritten as:

$$\frac{dC^\Omega}{dx_i^e} = 2 \frac{d\mathbf{f}_f^T}{dx_i^e} \mathbf{d}_f - \mathbf{d}_g^T \frac{d\mathbf{K}}{dx_i^e} \mathbf{d}, \quad i = x, r, t \quad (32)$$

Because compliance calculations require no applied force (see Section 2.2.2), this equation, expressed at elemental level, simplifies to:

$$\frac{dC^\Omega}{dx_i^e} = -\mathbf{d}^T \frac{d\mathbf{K}}{dx_i^e} \mathbf{d} = -\mathbf{d}^{eT} \frac{d\mathbf{K}^e}{dx_i^e} \mathbf{d}^e, \quad i = x, r, t \quad (33)$$

2.4. Solution algorithm

The optimization problem stated in Eqs. (10)–(15) is solved with the following algorithm:

1. Start with an initial guess for the design variables (\mathbf{x}).
2. Form the element stiffness matrices, \mathbf{K}^e , and assemble them into the global stiffness matrix \mathbf{K} .
3. Solve Eq. (18) for unknown displacement \mathbf{d}_f and unknown force (reaction) \mathbf{f}_g .
4. Compute the sensitivity of the objective function in Eq. (10) and constraints in Eqs. (11) and (12) with respect to the design variables \mathbf{x} using Eqs. (25)–(28) and (33).
5. Update the design variables using the Method of Moving Asymptotes (MMA) (Svanberg, 1987, 1995).
6. Check convergence; if not converged and the iteration not exceeded maximum iteration, for Example 200, go to step (2).
7. Check continuation step for η (and β if $\omega_p \neq 0$); if this (these) parameter(s) has (have) not reached its (their) maximum value(s) and a satisfactory solution is not reached do continuation step on that (those) parameter(s) and go to step (2).
8. If there is any element with $x_x^e < x_{xmin}$ remove those elements from design domain, reset η (and β if $\omega_p \neq 0$) to its (their) initial value(s), and go to step (1); otherwise stop,

where in step (8), x_{xmin} is a small number, for example 0.001, used as a threshold to remove inefficient elements from the periodic lattice. One may notice that the same constant threshold for element removal can be applied for any combinations of compressive and shear stiffness constraints. This is a clear advantage of utilizing the variable \mathbf{x}_x for element removal (the bounds on \mathbf{x}_x are always 0/1, regardless of the applied stiffness constraints).

In all problems, MMA, which is efficient for a large scale optimization problem with few constraints, starts from a uniform distribution of design variables, for example

$x_i^e = 1 \forall e \in \Omega$ and $i = x, r, t$, in step (1). A number of different initial guesses are also utilized for each optimization problem as explained in Section 3.2. Finally, notice that this specific optimizer requires the application of fixed bounds on each design variable. Therefore, the proposed definition for the thickness variable in Eq. (5) avoids the need of imposing the additional constraint $t^e \leq r^e$, as the radius changes. It is noted that we can use any gradient-based optimizer instead of MMA in step (5).

3. Minimum density 2D lattices with prescribed Young's and Shear moduli

The optimization algorithm described in Section 2 (Eqs. (10)–(15)) is applied to the investigation of the optimal topology of 2D periodic lattices for minimum relative density under simultaneous enforcement of compressive and shear stiffness constraints (i.e., specified minimum acceptable values of Young's and Shear moduli). The cross-section of each lattice member is assumed to be circular and hollow, and the base material is isotropic with Poisson's ratio (ν) equal to 0.3. The effect of the magnitude of the applied compressive and shear stiffness constraints on the optimal topology (and the minimum density) of the lattices is initially discussed. Subsequently, the effects of mesh connectivity, domain size aspect ratio, mesh density, maximum allowable element radius and coefficient of penalization on number of elements are investigated.

The Young's and shear moduli constraints in Eqs. (11) and (12), i.e. α_E and α_G , are chosen to be all possible combinations of $\{10^{-1}, 10^{-2}, 10^{-3}, 10^{-4}, 10^{-5}, 10^{-6}\}$, requiring the solution of a total of 36 optimization problems. For the calculations of Young's and Shear Modulus, the boundary conditions stated by Eqs. (21)–(22) and Eqs. (23)–(24) – suitably reduced to the 2D case (see Fig. 1) – are applied, respectively. For each optimization iteration, two finite element analyses are performed, one to impose the Young's modulus constraint and one to impose the shear modulus constraint.

The penalization coefficient against the number of elements in the final mesh (Eq. (10)) obviously has a large effect on the optimal designs (both in terms of optimal relative density and optimal architecture). Although a full investigation of the effect of this parameter on the optimal lattice topologies is beyond the scope of this investigation, a suitable value for this parameter is chosen as follows. Optimization problems are solved for the cases $\omega_p = 0$, $\omega_p = 0.001$, and $\omega_p = 0.01$. Not surprisingly, the simplicity of the optimal topology is proportional to the value of ω_p ; but although the relative densities (objective function) for the cases $\omega_p = 0$ and $\omega_p = 0.001$ are nearly identical (with the latter having 80% fewer elements in the final unit cell architecture), designs obtained with $\omega_p = 0.01$ are considerably heavier. Hence, a value of $\omega_p = 0.001$ is used for all subsequent calculations.

3.1. Initial mesh

As discussed in Section 2.2.2, only a quarter of a unit cell is modeled, thus imposing two axes of symmetry on the unit cell topology. Two fundamentally different initial mesh topologies are possible: (a) a locally connected mesh (Fig. 2(a)), where lattice nodes are connected by vertical, horizontal, and diagonal lattice elements to their nearest neighbors with every other node in the horizontal and vertical directions is missing the diagonal connections, and (b) a fully connected mesh (Fig. 2(b)), where each pair of nodes is connected by one element (overlapping elements are removed as needed). The specific mesh illustrated in Fig. 2(a) has 11×11 lattice nodes, for a total of 320 lattice elements. The fully connected mesh in Fig. 2(b) consists of a 5×5 -node lattice, for a total of 240 lattice elements. To attempt a meaningful comparison,

the number of the nodes in each mesh is chosen to result in roughly equivalent number of elements. Mesh sensitivity studies on both ground structures are reported in Appendix. For both meshes, each individual lattice element is modeled with a single Timoshenko beam finite element; the maximum radius, r_{max} , is set to $L_{min}^e/5$ and maintained fixed during the optimization, where L_{min}^e is the length of shortest element within the mesh, to ensure that the Timoshenko beam theory can be applied. The locally connected mesh automatically guarantees that elements cross only at the lattice nodes on the square grid, whereas in the fully connected mesh a large number of additional element crossings appear; for the sake of simplicity, only crossings that occur at the square lattice grid points are assumed to be lattice nodes. This simplification is conservative, in the sense that introducing lattice nodes at each crossing would result in a stiffer structure.

3.2. Minimum density designs

Fig. 3 displays one quarter of the optimized unit cells for select combinations of α_E and α_G , for the locally connected mesh in Fig. 2(a). Clearly, very few elements remain in the final domain. The color of the element represents its cross-sectional area (blue = thin, red = thick). Different color scalings are used for different optimized designs, and thus members with the same color in different optimized designs do not necessarily have the same cross-sectional area. Notice that in Fig. 3(a) all elements in each topology have the same cross-sectional area, while in Fig. 3(b) two groups of elements emerge: a group of “weak” elements (blue), and a group of “strong” elements (red). Often an extra group of intermediate elements develops, as illustrated in Fig. 3(c). Moreover, in a few optimized designs, the cross-sectional area of elements changes along collinear elements, resembling a continuous taper, as shown in Fig. 3(d) along the vertical elements.

Fig. 4 displays one quarter of the optimized unit cells for select combinations of α_E and α_G , for the fully connected mesh in Fig. 2(b). Similarly to the previous mesh connectivity, in some optimized designs, only one group of elements exist, see e.g. Fig. 4(a); in most of them, two groups of “weak” and “strong” elements develops, as shown in Fig. 4(b); and finally, in some designs, three groups of elements emerge (“weak”, “intermediate” and “strong”), as shown in Fig. 4(c). Also for this mesh connectivity, examples of collinear elements with varying cross-sectional area appear, as shown in the diagonal elements in Fig. 4(d).

Optimal topologies are extracted for all combinations of (α_E, α_G) , using uniform initial guesses based on the ground topologies shown in Fig. 2. Some combinations of parameters resulted in relatively simple topologies, whereas others yielded much more complex designs. To minimize the risk of converging to local minima, for each combination of (α_E, α_G) , the optimization process is subsequently repeated using the optimal topologies for all other (α_E, α_G) combinations as initial guesses. The topology with the minimum objective function is then chosen as the final solution for each (α_E, α_G) . We notice that although this procedure allows dramatic simplification of the optimal topologies, for every case in which the initial optimal topology is replaced with a simpler one, the density of the final design is very close to that of the initial optimum, confirming that this problem possesses a number of local minima with nearly equivalent performance.

Some general observations can be drawn from the optimal designs of Figs. 5 and 6. These conclusions hold for both mesh connectivities.

- Most topologies include two families of bars: vertical and diagonal members; the former are clearly efficient in compression, whereas the latter are optimal in shear. For situations where

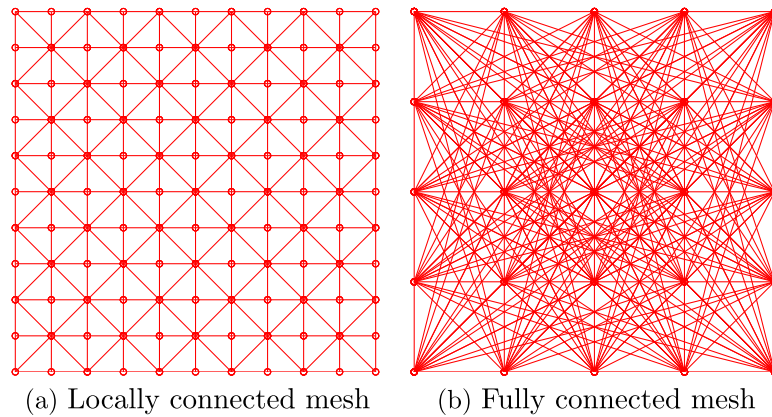


Fig. 2. Initial meshes used to model one quarter of a square unit cell; (a) locally connected mesh, where lattice nodes are connected by vertical, horizontal, and diagonal lattice elements to their nearest neighbors with every other node in the horizontal and vertical directions is missing the diagonal connections, (b) fully connected mesh, where each pair of nodes is connected by one element (overlapping elements are removed as needed).

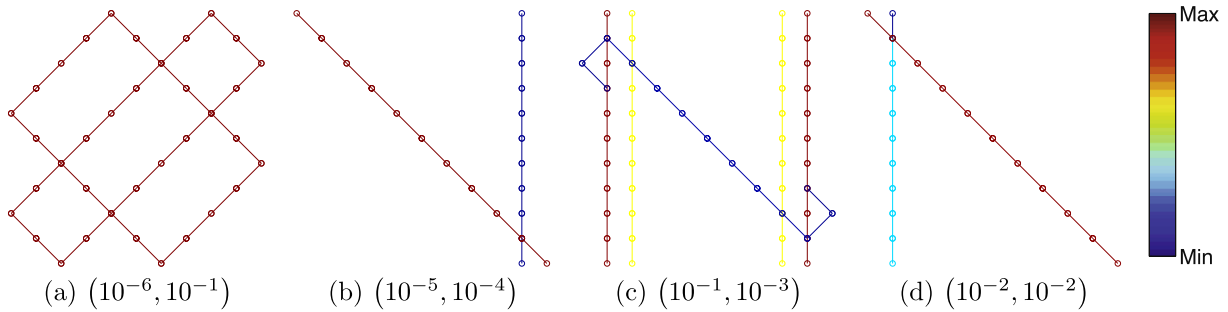


Fig. 3. One quarter of the optimized unit cells for select combinations of the pair (α_E, α_G) , for the locally connected mesh in Fig. 2(a). The color of the element represents its cross-section. Different color scalings are used for different optimized designs.

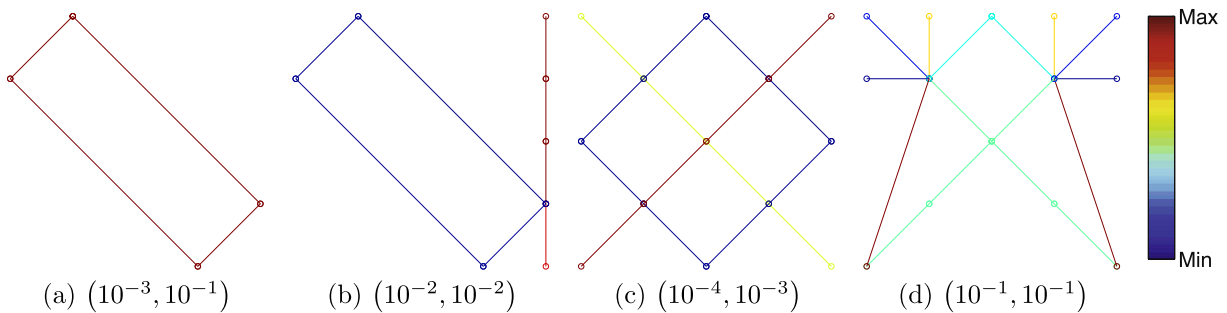


Fig. 4. One quarter of the optimized unit cells for select combinations of the pair (α_E, α_G) , for the fully connected mesh in Fig. 2(b). The color of the element represents its cross-section. Different color scalings are used for different optimized designs.

$\alpha_G \gg \alpha_E$, the bending stiffness of diagonal members is sufficient to meet the axial stiffness constraint on the lattice, and no vertical elements appear.

- Between 16% and 28% of optimized designs all elements have the same cross-sectional area, between 61% and 69% two groups of elements (“weak” and “strong”) develop, and for the remaining 11% to 14% of the cases, three groups of elements (“weak”, “intermediate” and “strong”) emerge.
- The same topology is optimal for all designs with the same ratio of shear to axial stiffness (i.e., same α_G/α_E) – albeit with different elements size – except for extremely stiff designs; for these cases, the upper bound on element areas is achieved and more complex optimal topologies are identified.

- There are few patterns that can be reproduced by swapping weak and strong elements, such as optimized designs for $(\alpha_E, \alpha_G) = (10^{-6}, 10^{-6})$ and $(\alpha_E, \alpha_G) = (10^{-6}, 10^{-5})$ in Fig. 5.
- Although not all elements in the same class (e.g., “strong”) have identically the same area, a clear banding of areas in one, two or three groups curiously appears, as clearly illustrated in Fig. 5.

Finally, notice that the existence of non-strong elements in the optimal solution (particularly at high stiffness), in spite of the penalization they receive from ω_p in Eq. (10), is a testament of the structural benefit of hierarchy and complexity. Moreover, it is worth mentioning that the vast majority of these optimized

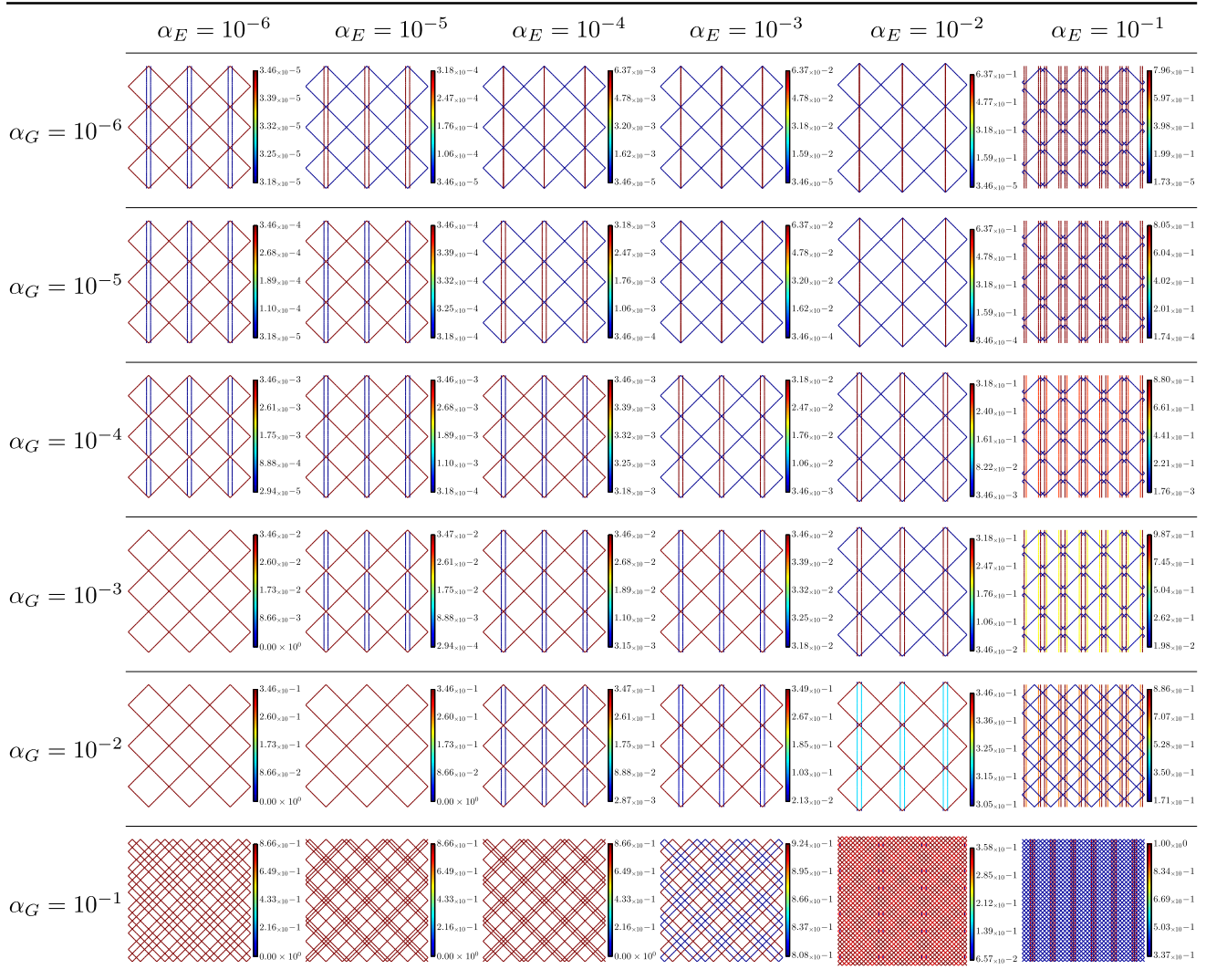


Fig. 5. 3×3 optimized patterns produced by replication of the optimized symmetric unit cell patterns for all combinations of the pair (α_E, α_G) for the locally connected mesh shown in Fig. 2(a). The color of the element represents its cross-sectional area (blue = thin, red = thick). Different color scalings are used for different optimized designs. Each color bar displays the cross-sectional area of each element, normalized with maximum allowable area, i.e. πr_{\max}^2 . (For interpretation of the references to color in this figure legend, the reader is referred to the web version of this article.)

designs are stretching dominated lattices, for which the shape of the member cross-section is inconsequential. Hence the results and conclusions of this work can be applied almost identically to 2D lattices of any cross-section.

The relative density of optimized lattices for the local mesh connectivity is displayed in Fig. 7. Although the actual lattice topologies are significantly different for the local and full mesh connectivities (see Figs. 5 and 6), the relative densities are essentially identical in both cases and the density map for the full connectivity mesh would be indistinguishable from that of Fig. 7. For both mesh connectivities, most of equipotential contour lines in Fig. 7 are slightly longer along the α_E axis, indicating that the shear constraint is generally harder to satisfy. For all combinations of (α_E, α_G) , the shear constraint is active, while for specific combinations, the axial stiffness constraint can be inactive. This is the reason why the same design emerges for the first four optimized patterns in the last row of Fig. 5. For example, the optimized design for $(\alpha_E, \alpha_G) = (10^{-6}, 10^{-1})$ in Fig. 5 is axially about 900 times stiffer than required.

Fig. 8 displays the ratio of the axial moduli in the unconstrained (X) and constrained (Y) directions for the optimized designs shown in Figs. 5 and 6. Notice that optimized lattices with high shear to axial stiffness ratio, i.e. $\alpha_G \geq \alpha_E$, have nearly cubic symmetry. This is due to the fact that these lattices possess strong diagonal elements, which provide equal axial stiffness in the X and Y direction by bending. On the contrary, for topologies with $\alpha_G < \alpha_E$, these diagonal members are weak and their effect on axial stiffness becomes negligible compared to that of the axial members. As axial members are only aligned with the Y direction (for which constraints are applied), this results in enormous difference between the two axial moduli. As an example, optimized topologies for $\alpha_G \geq 10000\alpha_E$ (top left quadrant in Fig. 8) have the same axial moduli in both directions, whereas for $10,000\alpha_G \leq \alpha_E$ (bottom right quadrant in Fig. 8) the axial modulus in the X direction is more than four orders of magnitude lower than that in Y direction.

For further investigation on effects of the domain aspect ratio, the maximum cross-section radius, and the number of initial elements in the mesh, the reader is referred to Appendices A,B,C.

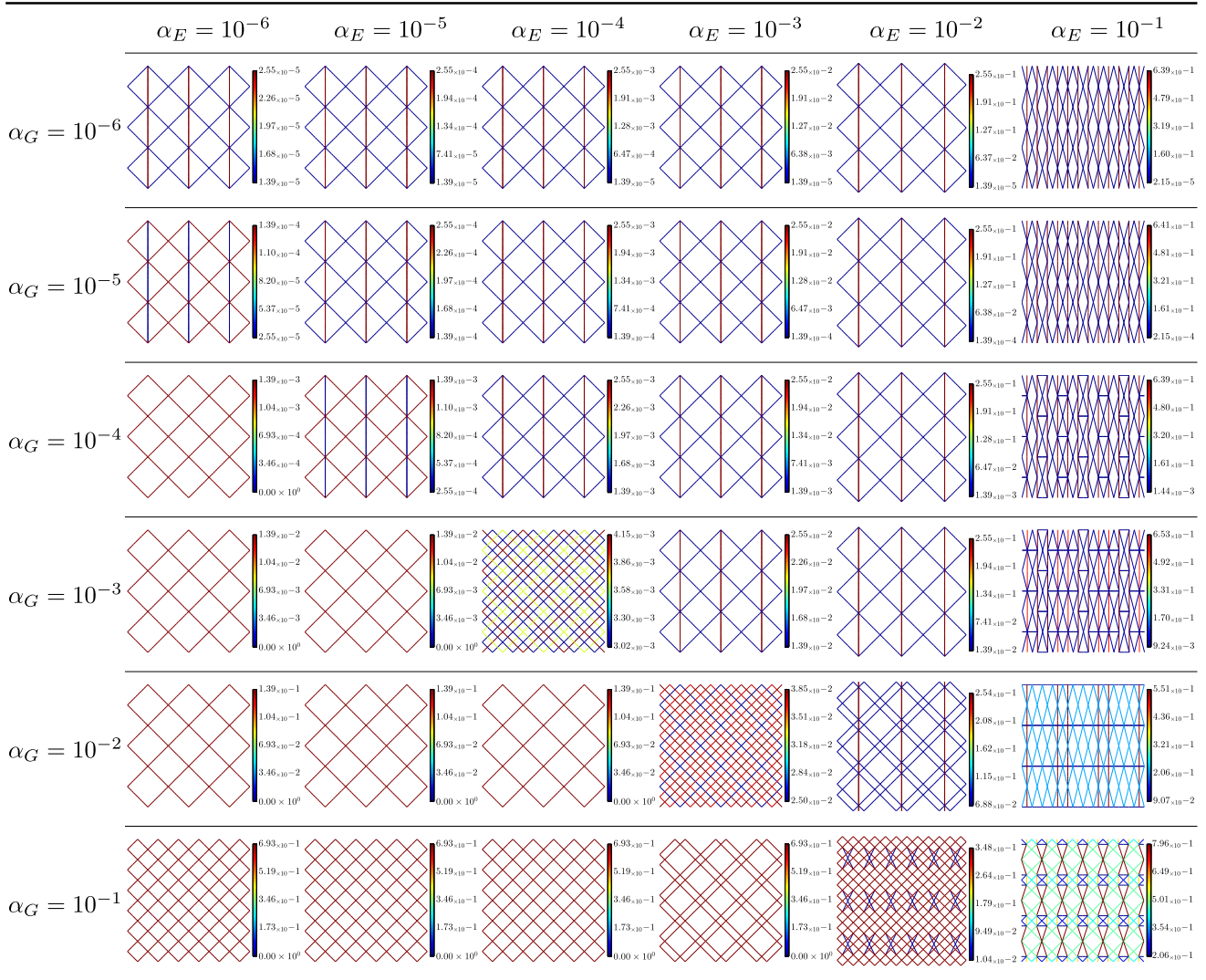


Fig. 6. 3×3 optimized patterns produced by replication of the optimized symmetric unit cell patterns for all combinations of the pair (α_E, α_G) using the fully connected mesh shown in Fig. 2(b). The color of the element represents its cross-sectional area (blue = thin, red = thick). Different color scalings are used for different optimized designs. Each color bar displays the cross-sectional area of each element, normalized with maximum allowable area, i.e. πr_{max}^2 . (For interpretation of the references to color in this figure legend, the reader is referred to the web version of this article.)

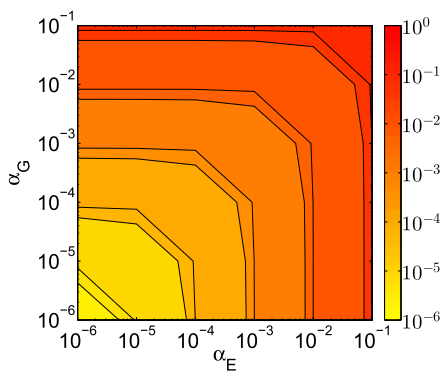


Fig. 7. Relative density, $\bar{\rho}$, of the optimized unit cells obtained using the locally and fully connected meshes in Fig. 2 for designs shown in Figs. 5 and 6.

3.3. Comparison with Hashin–Shtrickman bounds and classic isotropic lattices

In order to investigate the efficiency of the results shown in Fig. 5, we compare them with Hashin–Shtrickman (H–S) bounds

for isotropic two-phase (solid-void) composites, that can be obtained as follows (Hashin and Shtrickman, 1963):

$$\alpha_E^{HS} \leq \frac{\bar{\rho}}{3 - 2\bar{\rho}} \tag{34}$$

$$\alpha_G^{HS} \leq \frac{\bar{\rho}K}{(1 - \bar{\rho})(K + 2G) + K} \tag{35}$$

where α_E^{HS} and α_G^{HS} are the relative axial and shear moduli of the cellular material at the H–S bounds, respectively, G and K are the shear and the bulk moduli of the constituent material, respectively, and $\bar{\rho}$ denotes the relative density of the composite material.

As optimized designs shown in Figs. 5 and 6 are not required to be isotropic, this comparison helps quantifying the effect of anisotropy on the mechanical efficiency of the lattices. It is worth noticing that the hollow circular lattices discussed in this work are not proper 2D two-phase materials. Nonetheless, consider that for nearly any value of the shear or compressive stiffness constraints, the lattices are fundamentally stretching dominated (at least along the stiffer loading direction). As such, the stiffness contribution that arises from member bending is insignificant. This indicates that nearly the same stiffness can be achieved with prismatic

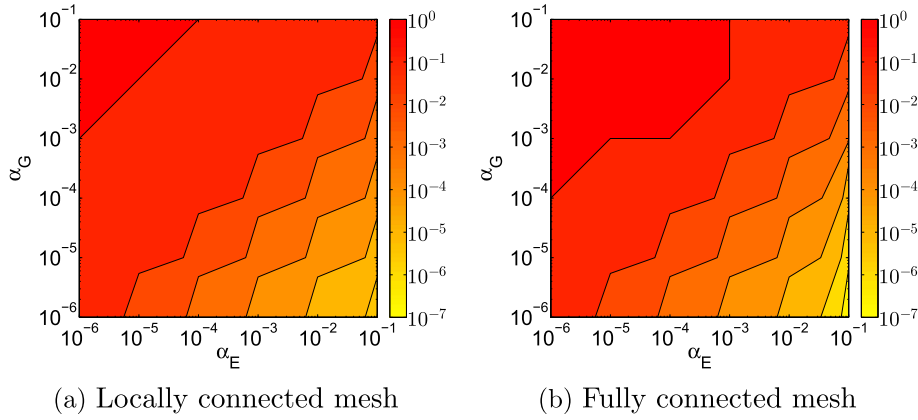


Fig. 8. Ratio of axial moduli of the lattice in the X and Y directions, $E_{lattice_x}/E_{lattice_y}$, with X the unconstrained direction and Y the constrained direction, for the optimized lattices shown in (a) Fig. 5; (b) Fig. 6.

cross-sections, where all the members have the same out-of-plane thickness. This would be equivalent to a 2D two-phase (solid–void) system, for which the H–S bounds would apply.

Fig. 9 shows the relative densities of the topology optimized lattices depicted in Fig. 5, normalized against the relative density of the H–S bounds. The key conclusion is that for all combinations of axial and shear moduli, the (not-necessarily isotropic) lattices obtained in this work (and depicted in Fig. 5) are more mechanical-ly efficient than the best (H–S) isotropic materials.

The dashed line in Fig. 9 illustrates the limit of existence for isotropic materials with Young’s and shear moduli simultaneously at the bound; that is, no isotropic material exists with combinations of relative Young’s and shear moduli that lie below this line; notice that this is the region where the optimized anisotropic lattices extracted in this work show the largest advantage over optimal isotropic lattices.

It is instructive to compare the performance of our optimized lattices with that of classic 2D lattice designs, in particular hexagonal, fully triangular, and Kagomé designs (Gibson and Ashby, 1999; Christensen, 1995).

This is accomplished in Fig. 10 for lattices with a relative density of $\bar{\rho} = 0.15$. The values of both moduli for hexagonal and fully triangular have been obtained by (Gibson and Ashby, 1999; Christensen, 1995)

$$\alpha_E^H = \frac{3}{2} \bar{\rho}^3 \quad (36)$$

$$\alpha_G^H = \frac{3(1+\nu)}{4} \bar{\rho}^3 \quad (37)$$

$$\alpha_E^{FT} = \frac{1}{3} \bar{\rho} \quad (38)$$

$$\alpha_G^{FT} = \frac{1+\nu}{4} \bar{\rho} \quad (39)$$

where α_E^H and α_G^H are relative axial and shear moduli of hexagonal design and α_E^{FT} and α_G^{FT} are relative axial and shear moduli of fully triangular design, respectively. It is worth mentioning that the elastic properties of a Kagomé design are the same as those of a fully triangular lattice (Christensen, 2000).

Obviously, Kagomé and fully triangular lattices are the most efficient in the group, as they are both stretching dominated architectures (the same is not true for the hexagonal design, that is bending dominated under the applied loads). Notice that the shape of the cross-section is important only for bending dominated lattices: a hollow cross-section (which would result in a more fair comparison with the lattices studied in this work) would elevate the stiffness of the hexagonal lattice beyond what displayed in Fig. 10, i.e. relative moduli obtained by Eqs. (36) and (37), without

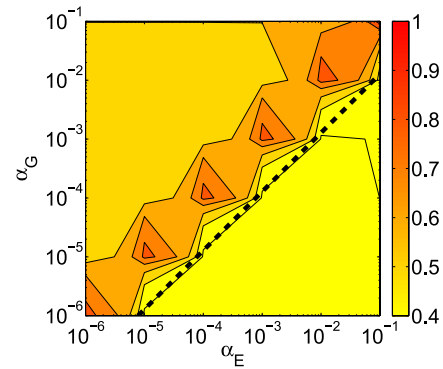


Fig. 9. Normalized relative density, $\bar{\rho}$, of the optimized unit cells shown in Fig. 5 against H–S bounds for isotropic two-phase (solid–void) composites. There exists no isotropic material whose Young’s modulus and shear modulus are at the bounds of elastic constraints represented in Eqs. (11) and (12) below the dashed line.

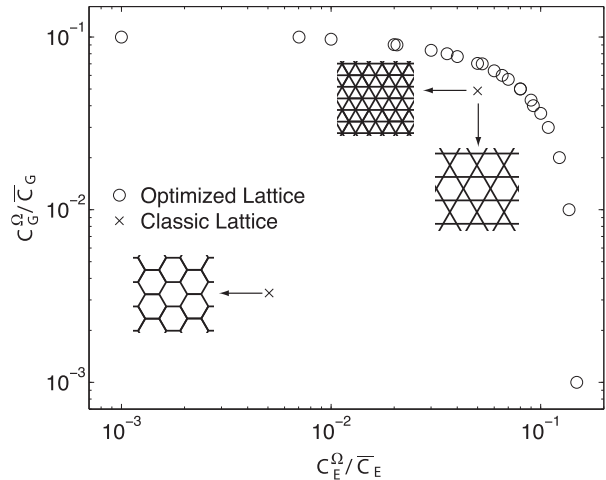


Fig. 10. Relative axial and shear moduli of hexagonal fully triangular and Kagomé lattices, together with the optimized lattices extracted using the proposed method. All lattices share the same relative density of 15%, i.e. $\bar{\rho} = 0.15$.

modifying the performance of the triangular and Kagomé lattice, i.e. relative moduli obtained by Eqs. (38) and (39). Nonetheless, the hexagonal lattice will always be less stiff than the other two isotropic designs. It is also worth mentioning that optimized anisotropic lattices with a relative density of 15% can be designed with the same Young’s modulus as a Kagomé lattice but with shear

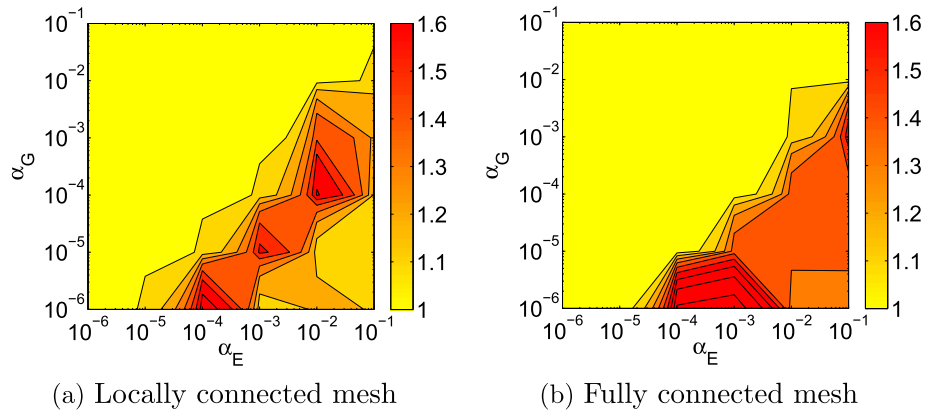


Fig. 11. Normalized relative density, $\bar{\rho}$, of the optimized unit cells with uniform thickness and radius obtained using (a) the locally connected mesh in Fig. 2(a); (b) the fully connected mesh in Fig. 2(b). All the values are normalized against corresponding values for optimized structures shown in Fig. 5.

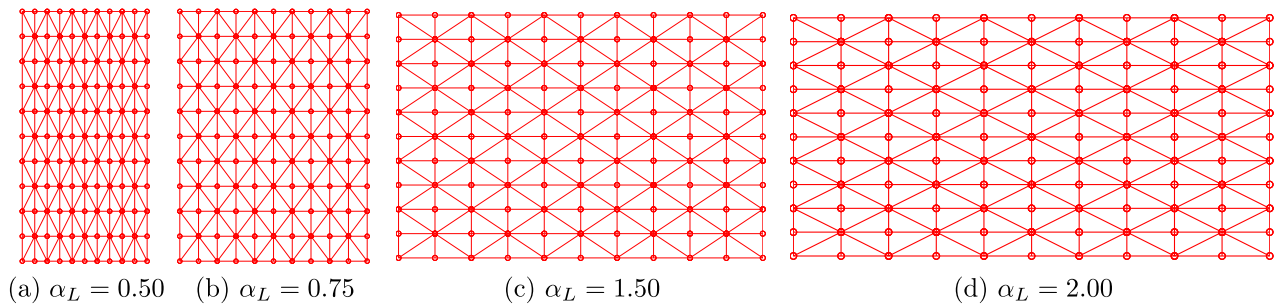


Fig. 12. Initial locally connected meshes used to model one quarter of a square unit cell with different domain aspect ratios.

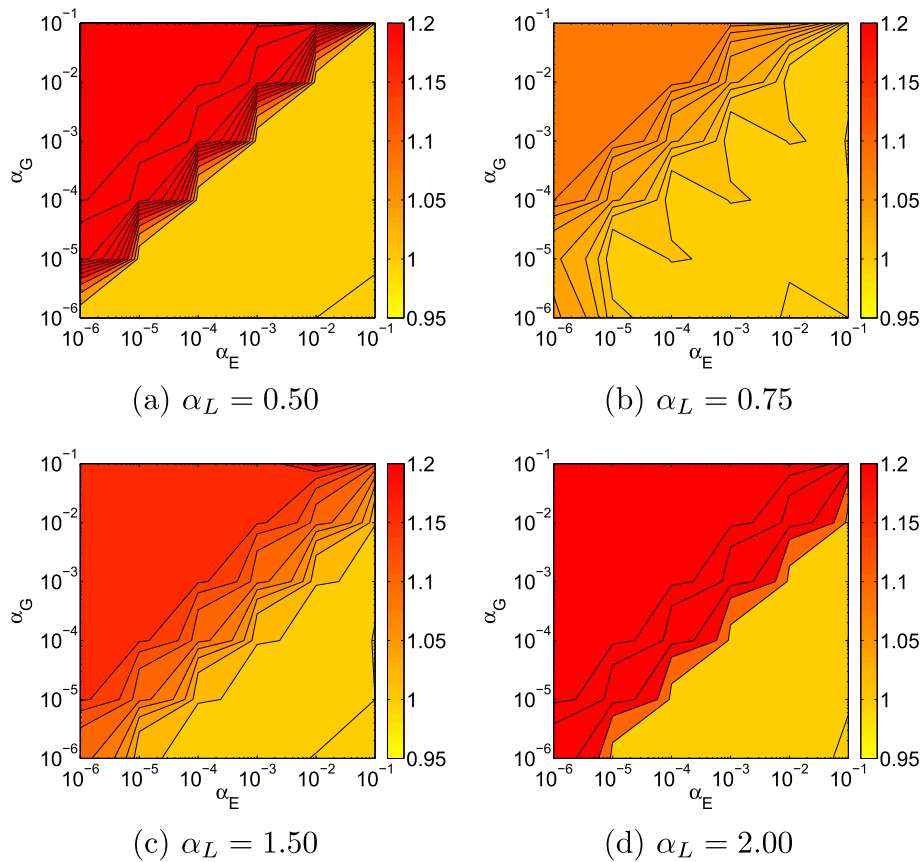


Fig. 13. Normalized relative density, $\bar{\rho}$, against corresponding relative density of the optimized unit cell for the square domain shown in Fig. 7 for optimized unit cells obtained using the initial fully connected meshes shown in Fig. 12.

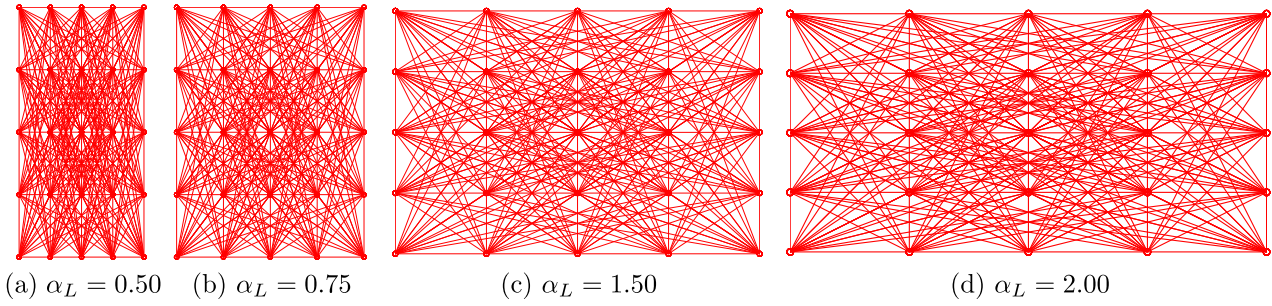


Fig. 14. Initial fully connected meshes used to model one quarter of a square unit cell with different domain aspect ratios.

modulus 44% higher; or alternatively, the same shear modulus but Young’s modulus 64% higher; or Young’s modulus and shear modulus 31% and 23% higher, respectively. Much larger benefits are possible for situations where the required shear modulus is much higher than the required Young’s modulus or viceversa.

3.4. Effect of hierarchy

Many of the optimal topologies in Figs. 5 and 6 are obviously hierarchical, i.e., they contain sub-lattices with elements of vastly different cross-sections. As manufacturing of hierarchical designs presents obvious challenges versus simpler geometries, it is instructive to assess the usefulness of hierarchy in achieving lightweight lattices with prescribed elastic properties. In order to probe the importance of topological hierarchy, we repeat the optimization studies leading to the topologies in Figs. 5 and 6, imposing the conditions that all elements in the lattice have the same radius and thickness, i.e., the same cross-sections.

The relative density of the uniform cross-section designs, normalized against the corresponding density of optimized hierarchical structures presented in Fig. 5, is depicted in Fig. 11. Notice that most optimized uniform cross-section topologies for combinations of axial and shear moduli where $\alpha_E \leq \alpha_G$ have similar or slightly larger relative densities comparing to hierarchical topologies. This is not surprising, as some topologies with $\alpha_E \leq \alpha_G$ in Figs. 5 and 6 already had uniform thickness and radius. On the other hand, for the region where $\alpha_E \gg \alpha_G$, using uniform cross-sections leads to significantly heavier designs (by more than 30%). The choice of initial mesh has a larger effect on the density of optimal uniform cross-section designs than for variable cross-section lattices. For locally connected meshes, optimized uniform cross-section structures with $\alpha_E \leq \alpha_G$ and $\alpha_E \gg \alpha_G$ are respectively 0.2% and 29.9% heavier than variable cross-section designs; these numbers change to 3.9% and 38.6% for the case of fully connected meshes.

From a manufacturing perspective, for the case $\alpha_E \leq \alpha_G$, optimized lattices with uniform cross-sections might be more

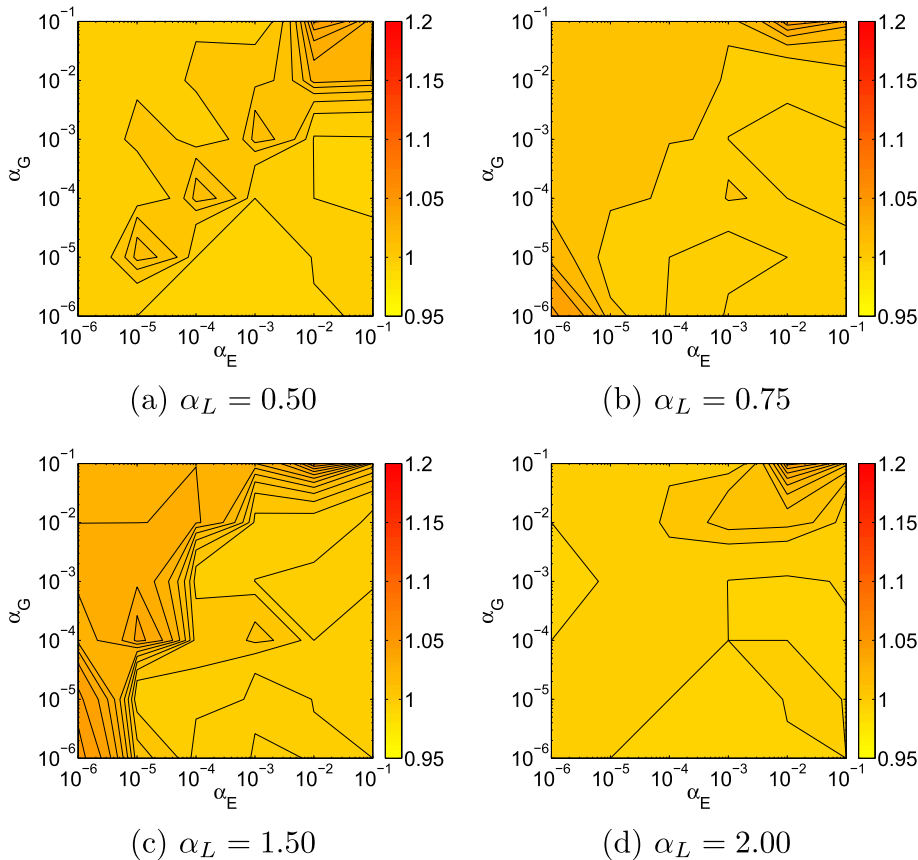


Fig. 15. Normalized relative density, $\bar{\rho}$, against corresponding relative density of the optimized unit cell for the square domain shown in Fig. 6 for optimized unit cells obtained using the initial fully connected meshes shown in Fig. 14.

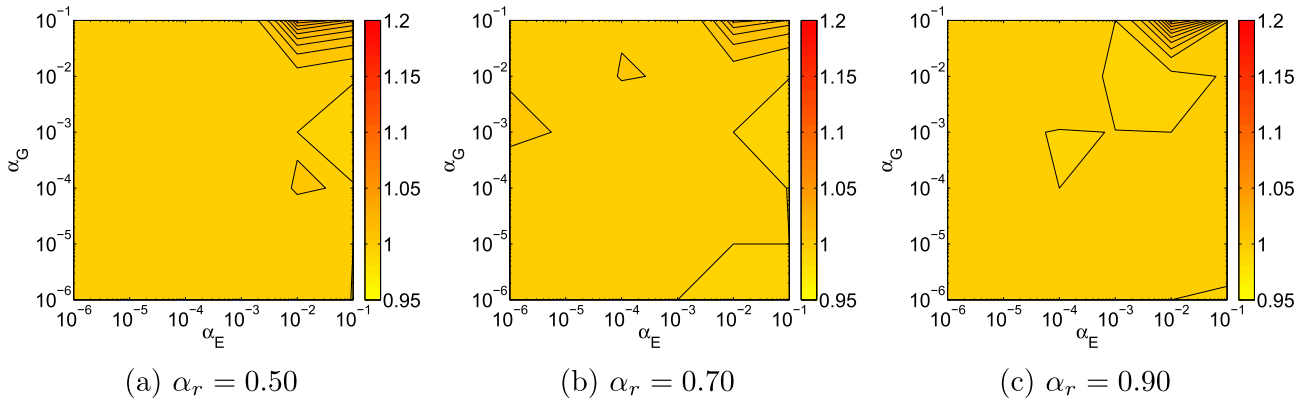


Fig. 16. Normalized relative density, $\bar{\rho}$, against corresponding relative density of the optimized unit cell for the designs shown in Fig. 6 for optimized unit cells obtained using the initial locally connected meshes shown in Fig. 2(a).

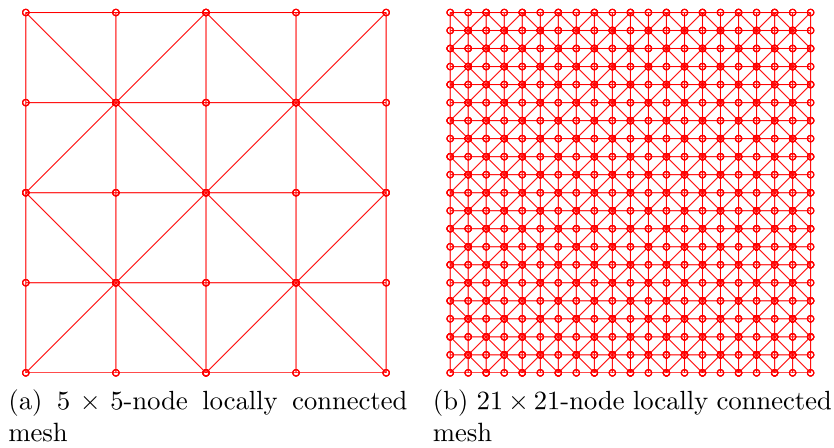


Fig. 17. Initial meshes used to model one quarter of a square unit cell; (a) A 5×5 -node locally connected mesh consisting of 56 beam elements, (b) A 21×21 -node locally connected mesh consisting of 1240 beam elements.

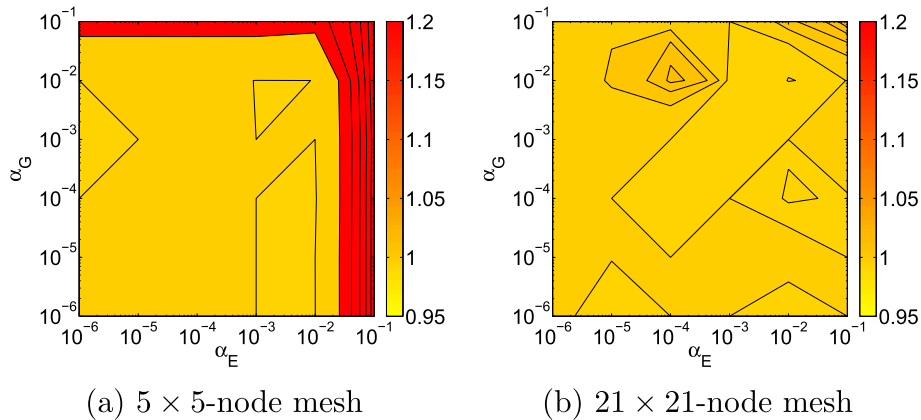


Fig. 18. Normalized relative density, $\bar{\rho}$, of the optimized unit cell using locally connected meshes shown in Fig. 17 with $r_{max} = L_x^2/100$. Relative density is normalized against the corresponding values for the optimized design using the locally connected mesh shown in Fig. 2(a) with the same r_{max} .

cost-effective than design with non-uniform thickness and radius, at nearly the same performance. This conclusion is not entirely obvious, though, as cross-section uniformity does not correlate with topological simplicity: most of the optimized unit cells for uniform cross-section designs on average have about three times more elements than for the non-uniform case. Ultimately, the optimal solution from a manufacturability standpoint will depend on the manufacturing approach used and the relative values of fabrication and material costs.

4. Conclusions

This paper investigates the optimal topology of lightweight two-dimensional periodic lattices under simultaneous axial and shear stiffness constraints. The stiffness analysis is performed with the finite elements method, on a unit cell consisting of a network of lattice elements modeled as Timoshenko beams with a hollow circular cross-section. The method for stiffness calculation is the same for 2D and 3D lattices, for both axial and shear stiffness, as

long as appropriate boundary conditions are adopted. For each choice of axial and shear stiffness constraints, minimum density lattice designs are identified with a topology optimization algorithm; starting from a dense mesh of elements, the algorithm systematically removes inefficient elements and resizes the cross-section of the remaining ones, finally converging to an optimal solution. The design variables in the optimization problem are existence of each element and the geometric variables related to the hollow tube cross-section, i.e., element thickness and radius. The objective function is the lattice relative density, weighted on the number of elements to simplify the optimized structure. The algorithm developed here is applied to the density minimization of 2D lattices subject to 36 combinations of axial and shear stiffness constraints, spanning six orders of magnitude on Young's and shear moduli of the lattice.

In the optimized topologies, three groups of architectures emerge: (i) architectures where all the elements have uniform cross-section (between 16% and 28% of the total); (ii) architectures with two distinct sub-lattices, each consisting of elements with uniform cross-section (between 61% and 69% of the total); and (iii) architectures with three or more distinct sub-lattices, each with its own uniform cross-section (between 11% and 14% of the total). Not surprisingly, the same topology is optimal for all designs with the same ratio of shear to axial stiffness (i.e., same α_G/α_E) – albeit with different elements size – except for extremely stiff designs; for these cases, the upper bound on element areas is achieved and more complex optimal topologies are identified. It is worth noting that even though all the elements within the final optimal solutions share the same penalization from ω_p regardless of their cross-section, the appearance of non-strong sub-lattices in the optimal designs shows their importance on the efficiency of the whole lattice and is ultimately a testament of the structural benefit of hierarchy and complexity.

By comparing the optimized solutions with the well-known H–S bounds, we show that the optimized topologies are consistently lighter than the best isotropic cellular materials (with weight savings between 67% and 5%). The advantage is more significant for required combinations of axial and shear stiffness that are unattainable by isotropic materials, i.e., requirements on the Young's modulus that are much more stringent than for the shear modulus. Furthermore, comparing optimized lattices with classic lattices, including hexagonal, triangular, and Kagomé designs, shows that for a relative density of 15%, the optimal latticed identified in this work can be designed with 64% higher Young's modulus for the same shear modulus, or 44% higher shear modulus for the same Young's modulus, or 31% and 23% higher Young's and shear modulus, respectively.

Next, we examine the effect of the emerging hierarchy in the optimized designs, by comparing the lattices extracted in this work with designs optimized in the presence of a uniform cross-section constraint. For conditions where $\alpha_E \leq \alpha_G$, the effect of hierarchy is negligible and uniform cross-section lattices perform nearly as well as hierarchical designs; in contrast, for the region where $\alpha_E \gg \alpha_G$, imposing cross-section uniformity results in significantly heavier designs.

Further mesh sensitivity studies are reported in Appendix. An investigation in the role of domain aspect ratio shows that square unit cells are most efficient if locally connected initial meshes are used, whereas the domain aspect ratio plays a negligible role in the case of fully connected initial meshes. It is also verified that the maximum cross-section radius adopted, i.e. r_{max} , and the number of initial elements (mesh density) have minimal effects on the optimized solutions.

This work shows that topologically optimized 2D lattices can be much more weight-efficient than conventional designs for

conditions where isotropy is not required, particularly when vastly different values of shear and Young's modulus are imposed. The algorithm presented here is equally applicable to the analysis of 3D lattices, although the visualization of optimal topologies becomes more cumbersome. Possible future extension of the present work will consider the problem of density minimization under simultaneous axial and shear strength constraints, as well as simultaneous applications of stiffness and strength constraints.

Acknowledgements

This work was financially supported by the Office of Naval Research under Grant No. N00014-11-1-0884 (program manager: D. Shifler). This support is gratefully acknowledged. The authors are also thankful to Krister Svanberg for providing the MMA optimizer subroutine. The computing support was partially provided by the High Performance Computing Cluster within the Office of Information Technology at the University of California, Irvine, which is gratefully acknowledged.

Appendix A. Effect of domain size aspect ratio

The design domains for the initial meshes depicted in Fig. 2 are square. It is interesting to explore the effect of the aspect ratio of the unit cell on the optimal topologies and relative densities. Fig. 12 shows locally connected initial meshes with four domain aspect ratios, i.e. $\alpha_L = L_X^\Omega/L_Y^\Omega = \{0.50, 0.75, 1.50, 2.00\}$. Fig. 13 depicts the relative density of optimized unit cells with different domain aspect ratios, for all combinations of (α_E, α_G) , normalized with the relative densities of the optimal topologies for the square domain. Locally connected unit cells are used for all calculations. For the locally connected initial mesh shown in Fig. 2(a), almost all the normalized relative densities are equal to or greater than 1, indicating that the square domain, $\alpha_L = 1.00$, provides the best optimized topologies. The heavier relative densities occur for $\alpha_E \leq \alpha_G$. In general, the farther the domain from a square, the heavier the resulting optimized topologies.

If a fully connected initial mesh is chosen (Fig. 14), the conclusions change. In this case, regardless of the aspect ratio of the domain, topologies with diagonal bars oriented at an angle close to 45° can always be extracted. As a result, the effect of the domain aspect ratio on the relative density of the optimized topologies is negligible (Fig. 15).

Appendix B. Effect of maximum radius (r_{max})

In each optimization, the maximum radius (r_{max}) is set to $I_{min}^e/5$. To explore the effect of this parameter, here we reduce the maximum radius by a reduction coefficient, α_r , varying from 0.50 to 0.90, and re-optimize the lattice designs for all combinations of the pair of (α_E, α_G) . As before, we optimize one quarter of the unit cell, using the initial locally connected mesh shown in Fig. 2(a). Fig. 16 illustrates the relative densities, normalized against the corresponding relative density of the optimized unit cell for the square domain shown in 6, for optimized unit cells with three different values of the radius reduction coefficient. The results clearly show that the effect of maximum radius is not significant: on average, applying a radius reduction coefficient equal to 0.50, 0.70, and 0.90 leads to designs that are 0.35%, 0.18%, and 0.17% denser than for the case $\alpha_r = 1.00$, respectively.

Appendix C. Effect of number of initial elements (initial n_{el})

The last parameter that is investigated is the initial mesh density, i.e., the number of initial elements in the mesh (initial n_{el}). In

order to study its effect, we use three different initial domains: (i) the initial 11×11 -node locally connected mesh shown in Fig. 2(a), consisting of 320 beam elements; (ii) a 5×5 -node locally connected mesh with 56 beam elements (Fig. 17(a)); and (iii) a 21×21 -node locally connected mesh, consisting of 1240 beam elements (Fig. 17(b)). For all three meshes, $r_{max} = L_X^0/100$ is chosen.

The relative densities of the optimized designs for the two meshes depicted in Fig. 17 (cases (ii) and (iii) above) are reported in Fig. 18, normalized by the relative densities of mesh (i). Notice that the optimized designs for the 5×5 -node locally connected mesh do not fulfill the stiffness constraint when either of α_E or α_G is equal to 10^{-1} ; but otherwise, these three meshes converge to the same relative density for all different combinations of (α_E, α_G) . The conclusion is that the results are not mesh density sensitive, and therefore, using a mesh with more nodes and elements is not required.

References

- Allen, Howard G., 1969. *Analysis and Design of Structural Sandwich Panels*, vol. 51. Pergamon Press, Oxford.
- Asadpoure, Alireza, Guest, James K., Valdevit, Lorenzo, 2014. Incorporating fabrication cost into topology optimization of discrete structures and lattices. *Struct. Multidiscip. Optim.* <http://dx.doi.org/10.1007/s00158-014-1133-8>.
- Bell, Dominik J., Tian Jian, Lu, Fleck, Norman A., Spearing, Simon M., 2005. MEMS actuators and sensors: observations on their performance and selection for purpose. *J. Micromech. Microeng.* 15 (7), S153–S164. <http://dx.doi.org/10.1088/0960-1317/15/7/022>.
- Bendsøe, Martin P., 1989. Optimal shape design as a material distribution problem. *Struct. Optim.* 1 (4), 193–202. <http://dx.doi.org/10.1007/BF01650949>.
- Bendsøe, Martin P., Sigmund, Ole, 2003. *Topology Optimization: Theory, Methods and Applications*. Springer.
- Bourgat, J.F., 1979. Numerical experiments of the homogenization method. In: Glowinski, R., Lions, J.L., Lioria, Iria (Eds.), *Computing Methods in Applied Sciences and Engineering*, Lecture Notes in Mathematics, vol. 704. Springer, Berlin, Heidelberg, pp. 330–356. <http://dx.doi.org/10.1007/BFb0063630>.
- Cadman, Joseph E., Zhou, Shiwei, Chen, Yuhang, Li, Qing, 2013. On design of multifunctional microstructural materials. *J. Mater. Sci.* 48 (1), 51–66. <http://dx.doi.org/10.1007/s10853-012-6643-4>.
- Christensen, Richard M., 1995. The hierarchy of microstructures for low density materials. In: Casey, James, Crochet, Marcel J. (Eds.), *Theoretical, Experimental, and Numerical Contributions to the Mechanics of Fluids and Solids*. Birkhäuser, Basel, pp. 506–521. <http://dx.doi.org/10.1007/978-3-0348-9229-227>.
- Christensen, Richard M., 2000. Mechanics of cellular and other low-density materials. *Int. J. Solids Struct.* 37 (1–2), 93–104. [http://dx.doi.org/10.1016/S0020-7683\(99\)00080-3](http://dx.doi.org/10.1016/S0020-7683(99)00080-3).
- Cowper, G.R., 1966. The shear coefficient in Timoshenko's beam theory. *J. Appl. Mech.* 33 (2), 335. <http://dx.doi.org/10.1115/1.3625046>.
- Deshpande, Vikram S., Fleck, Norman A., Ashby, Michael F., 2001. Effective properties of the octet-truss lattice material. *J. Mech. Phys. Solids* 49 (8), 1747–1769. [http://dx.doi.org/10.1016/S0022-5096\(01\)00010-2](http://dx.doi.org/10.1016/S0022-5096(01)00010-2).
- Dobson, David C., Cox, Steven J., 1999. Maximizing band gaps in two-dimensional photonic crystals. *SIAM J. Appl. Math.* 59 (6), 2108–2120. <http://dx.doi.org/10.1137/S0036139998338455>.
- Dorn, William S., Gomory, Ralph E., Greenberg, Herbert J., 1964. Automatic design of optimal structures. *J. Mec.* 3 (1), 25–52.
- Evans, Anthony G., He, MingYuan, Deshpande, Vikram S., Hutchinson, John W., Jacobsen, Alan J., Carter, William B., 2010. Concepts for enhanced energy absorption using hollow micro-lattices. *Int. J. Impact Eng.* 37 (9), 947–959. <http://dx.doi.org/10.1016/j.ijimpeng.2010.03.007>.
- Evans, Anthony G., Hutchinson, John W., Fleck, Norman A., 2001. The topological design of multifunctional cellular metals. *Prog. Mater. Sci.* 46 (3–4), 309–327. [http://dx.doi.org/10.1016/S0079-6425\(00\)00016-5](http://dx.doi.org/10.1016/S0079-6425(00)00016-5).
- Gibson, Ian, Rosen, David W., Stucker, Brent, 2010. *Additive Manufacturing Technologies*. Springer, Boston, MA, US. <http://dx.doi.org/10.1007/978-1-4419-1120-9>.
- Gibson, Lorna J., Ashby, Michael F., 1999. *Cellular Solids: Structure and Properties*, second ed. Cambridge University Press, UK.
- Guedes, JoséMiranda, Kikuchi, Noboru, 1990. Preprocessing and postprocessing for materials based on the homogenization method with adaptive finite element methods. *Comput. Methods Appl. Mech. Eng.* 83 (2), 143–198. [http://dx.doi.org/10.1016/0045-7825\(90\)90148-F](http://dx.doi.org/10.1016/0045-7825(90)90148-F).
- Guest, James K., Prévost, Jean H., Belytschko, Ted B., 2004. Achieving minimum length scale in topology optimization using nodal design variables and projection functions. *Int. J. Numer. Methods Eng.* 61 (2), 238–254. <http://dx.doi.org/10.1002/nme.1064>.
- Hashin, Zvi, Shtrikman, Shmuel, 1963. A variational approach to the theory of the elastic behaviour of multiphase materials. *J. Mech. Phys. Solids* 11 (2), 127–140. [http://dx.doi.org/10.1016/0022-5096\(63\)90060-7](http://dx.doi.org/10.1016/0022-5096(63)90060-7).
- Hyun, Sangil, Torquato, Salvatore, 2002. Optimal and manufacturable two-dimensional, Kagomé-like cellular solids. *J. Mater. Res.* 17 (01), 137–144. <http://dx.doi.org/10.1557/JMR.2002.0021>.
- Jacobsen, Alan J., Barvosa-Carter, William, Nutt, Steven, 2007. Micro-scale truss structures formed from self-propagating photopolymer waveguides. *Adv. Mater.* 19 (22), 3892–3896. <http://dx.doi.org/10.1002/adma.200700797>.
- Li, Shuguang, 2008. Boundary conditions for unit cells from periodic microstructures and their implications. *Compos. Sci. Technol.* 68 (9), 1962–1974. <http://dx.doi.org/10.1016/j.compscitech.2007.03.035>.
- Liu, Ling, Yan, Jun, Cheng, Gengdong, 2008. Optimum structure with homogeneous optimum truss-like material. *Comput. Struct.* 86 (13–14), 1417–1425. <http://dx.doi.org/10.1016/j.compstruc.2007.04.030>.
- Maloney, Kevin J., Roper, Christopher S., Jacobsen, Alan J., Carter, William B., Valdevit, Lorenzo, Schaedler, Tobias A., 2013. Microlattices as architected thin films: analysis of mechanical properties and high strain elastic recovery. *APL Mater.* 1 (2), 022–106. <http://dx.doi.org/10.1063/1.4818168>.
- Niu, Fei, Shengli, Xu, Gengdong, Cheng, 2011. A general formulation of structural topology optimization for maximizing structural stiffness. *Struct. Multidiscip. Optim.* 43 (4), 561–572. <http://dx.doi.org/10.1007/s00158-010-0585-8>.
- Paulino, Glaucio H., Nelli Silva, Emílio Carlos, Le, Chau H., 2009. Optimal design of periodic functionally graded composites with prescribed properties. *Struct. Multidiscip. Optim.* 38 (5), 469–489. <http://dx.doi.org/10.1007/s00158-008-0300-1>.
- Rozvany, George I.N., 1996. Difficulties in truss topology optimization with stress, local buckling and system stability constraints. *Struct. Optim.* 11 (3–4), 213–217. <http://dx.doi.org/10.1007/BF01197036>.
- Rozvany, George I.N., Zhou, Ming, Birker, Torben, 1992. Generalized shape optimization without homogenization. *Struct. Optim.* 4 (4), 250–252. <http://dx.doi.org/10.1007/BF01742754>.
- Schaedler, Tobias A., Jacobsen, Alan J., Torrents, Anna, Sorensen, Adam E., Lian, Jie, Greer, Julia R., Valdevit, Lorenzo, Carter, William B., 2011. Ultralight metallic microlattices. *Science (New York, NY)* 334 (6058), 962–965.
- Sigmund, O., Torquato, S., 1997. Design of materials with extreme thermal expansion using a three-phase topology optimization method. *J. Mech. Phys. Solids* 45 (6), 1037–1067. [http://dx.doi.org/10.1016/S0022-5096\(96\)00114-7](http://dx.doi.org/10.1016/S0022-5096(96)00114-7).
- Sigmund, Ole, 1994. Materials with prescribed constitutive parameters: an inverse homogenization problem. *Int. J. Solids Struct.* 31 (17), 2313–2329. [http://dx.doi.org/10.1016/0020-7683\(94\)90154-6](http://dx.doi.org/10.1016/0020-7683(94)90154-6).
- Sigmund, Ole, 1995. Tailoring materials with prescribed elastic properties. *Mech. Mater.* 20 (4), 351–368. [http://dx.doi.org/10.1016/0167-6636\(94\)00069-7](http://dx.doi.org/10.1016/0167-6636(94)00069-7).
- Sigmund, Ole, Jensen, Jakob S., 2003. Systematic design of phononic band-gap materials and structures by topology optimization. *Philos. Trans. Ser. A, Math. Phys. Eng. Sci.* 361 (1806), 1001–1019. <http://dx.doi.org/10.1098/rsta.2003.1177>.
- Silva, E.C. Nelli, Ono Fonseca, J.S., Kikuchi, Noboru, 1997. Optimal design of piezoelectric microstructures. *Comput. Mech.* 19 (5), 397–410. <http://dx.doi.org/10.1007/s004660050188>.
- Svanberg, Krister, 1987. The method of moving asymptotes – a new method for structural optimization. *Int. J. Numer. Methods Eng.* 24 (2), 359–373. <http://dx.doi.org/10.1002/nme.1620240207>.
- Svanberg, Krister, 1995. A globally convergent version of MMA without linesearch. In: Olhoff, Niels, Rozvany, George I.N. (Eds.), *Proceedings of the First World Congress of Structural and Multidisciplinary Optimization*. Pergamon Press, Elmsford, NY, pp. 6–16.
- Valdevit, Lorenzo, Godfrey, Scott W., Schaedler, Tobias A., Jacobsen, Alan J., Carter, William B., 2013. Compressive strength of hollow microlattices: Experimental characterization, modeling, and optimal design. *J. Mater. Res.* 28 (17), 2461–2473. <http://dx.doi.org/10.1557/jmr.2013.160>.
- Valdevit, Lorenzo, Hutchinson, John W., Evans, Anthony G., 2004. Structurally optimized sandwich panels with prismatic cores. *Int. J. Solids Struct.* 41 (18–19), 5105–5124. <http://dx.doi.org/10.1016/j.ijsolstr.2004.04.027>.
- Valdevit, Lorenzo, Jacobsen, Alan J., Greer, Julia R., Carter, William B., 2011. Protocols for the optimal design of multi-functional cellular structures: from hypersonics to micro-architected materials. *J. Am. Ceram. Soc.* 94, s15–s34. <http://dx.doi.org/10.1111/j.1551-2916.2011.04599.x>.
- Valdevit, Lorenzo, Pantano, A., Stone, Howard A., Evans, Anthony G., 2006a. Optimal active cooling performance of metallic sandwich panels with prismatic cores. *Int. J. Heat Mass Transfer* 49 (21–22), 3819–3830. <http://dx.doi.org/10.1016/j.jheatmasstransfer.2006.03.042>.
- Valdevit, Lorenzo, Vermaak, Natasha, Zok, Frank W., Evans, Anthony G., 2008. A Materials Selection Protocol for Lightweight Actively Cooled Panels. *J. Appl. Mech.* 75 (6), 061. <http://dx.doi.org/10.1115/1.2966270>, pp. 061, 022.
- Valdevit, Lorenzo, Wei, Zhensong, Mercer, Christopher, Zok, Frank W., Evans, Anthony G., 2006b. Structural performance of near-optimal sandwich panels with corrugated cores. *Int. J. Solids Struct.* 43 (16), 4888–4905. <http://dx.doi.org/10.1016/j.ijsolstr.2005.06.073>.
- Wadley, Haydn N.G., Dharmasena, Kumar P., He, MingYuan, McMeeking, Robert M., Evans, Anthony G., Bui-Thanh, Tan, Radovitzky, Raúl A., 2010. An active concept for limiting injuries caused by air blasts. *Int. J. Impact Eng.* 37 (3), 317–323. <http://dx.doi.org/10.1016/j.ijimpeng.2009.06.006>.
- Wang, Fengwen, Sigmund, Ole, Jensen, Jakob S., 2014. Design of materials with prescribed nonlinear properties. *J. Mech. Phys. Solids* 69, 156–174. <http://dx.doi.org/10.1016/j.jmps.2014.05.003>.

- Yan, Jun, Cheng, Gengdong, Liu, Shutian, Liu, Ling, 2006. Comparison of prediction on effective elastic property and shape optimization of truss material with periodic microstructure. *Int. J. Mech. Sci.* 48 (4), 400–413. <http://dx.doi.org/10.1016/j.ijmecsci.2005.11.003>.
- Zok, Frank W., Rathbun, Howard J., He, MingYuan, Ferri, Enrico, Mercer, Christopher, McMeeking, Robert M., Evans, Anthony G., 2005. Structural performance of metallic sandwich panels with square honeycomb cores. *Philos. Mag.* 85 (26–27), 3207–3234. <http://dx.doi.org/10.1080/14786430500073945>.
- Zok, Frank W., Rathbun, Howard J., Wei, Zhensong, Evans, Anthony G., 2003. Design of metallic textile core sandwich panels. *Int. J. Solids Struct.* 40 (21), 5707–5722. [http://dx.doi.org/10.1016/S0020-7683\(03\)00375-5](http://dx.doi.org/10.1016/S0020-7683(03)00375-5).
- Zok, Frank W., Waltner, Seth A., Wei, Zhensong, Rathbun, Howard J., McMeeking, Robert M., Evans, Anthony G., 2004. A protocol for characterizing the structural performance of metallic sandwich panels: application to pyramidal truss cores. *Int. J. Solids Struct.* 41 (22–23), 6249–6271. <http://dx.doi.org/10.1016/j.ijsolstr.2004.05.045>.